



# Energetics of interannual temperature variability

Jouni Räisänen<sup>1</sup>

Received: 29 September 2017 / Accepted: 15 June 2018 / Published online: 18 June 2018  
© Springer-Verlag GmbH Germany, part of Springer Nature 2018

## Abstract

Energetics of interannual temperature variability in the years 1980–2016 is studied using two reanalysis data sets. Monthly temperature anomalies are decomposed to contributions from the net surface energy flux, atmospheric energy convergence minus storage (CONV), and processes that affect the top-of-the-atmosphere radiation balance. The analysis reveals a strong compensation between the net surface heat flux and CONV over the ice-free oceans, with the former driving the temperature variability over the tropical oceans and the latter at higher latitudes. CONV also makes a dominant contribution to temperature anomalies in the winter hemisphere extratropical continents. During the summer half-year and in the tropics, however, variations in cloudiness dominate the temperature variability over land, while the contribution of CONV is modest or even negative. The latter reflects the diffusion-like behaviour of short-term atmospheric variability, which acts to spread out the local, to a large extent cloud-induced temperature anomalies to larger areas. The ERA-Interim and MERRA2 reanalyses largely agree on the general energy budget features of interannual temperature variability, although substantial quantitative differences occur in some of the individual terms.

**Keywords** Temperature variability · Energy budget · Reanalysis · ERA-Interim · MERRA2

## 1 Introduction

Interannual variations in climate are of great practical importance. In particular, extended periods of anomalously hot or cold weather have large impacts on nature and society. Recent prominent examples include the heat waves in central Europe in 2003 (García-Herrera et al. 2010) and in Russia in 2010 (Barriopedro et al. 2011), and the cold winter in eastern North America in 2013–2014 (Yu and Zhang 2015). Nonetheless, such extremes are just the tip of the iceberg within an omnipresent continuum of temperature variability, the magnitude of which depends on both the season and the location. The largest interannual temperature variability is observed over ice-covered oceans and high-latitude continents in winter, whereas the variability over

the low-to-mid-latitude oceans is relatively muted outside of the eastern Tropical Pacific (Holmes et al. 2016; see also Figs. 3a, and 4a, b).

A fraction of interannual temperature variability is driven by external forcing such as major volcanic eruptions (Robock 2000; Paik and Min 2017). However, most of it results from the chaotic internal dynamics of the climate system: the variations in atmospheric and oceanic circulation, and the resulting perturbations in sea and land surface conditions. The influence of the oceans is largest at low latitudes, where the atmospheric circulation and temperatures are strongly controlled by the distribution of sea surface temperature (SST) (Wells 2012; Holton and Hakim 2012). In particular, the El Niño—La Niña variability in the eastern-to-central equatorial Pacific SSTs generates atmospheric teleconnections that profoundly affect the climate all around the tropics but to some extent also in extratropical latitudes (Diaz et al. 2001; Yang and DelSole 2012). However, the relative impact of SST variability decreases and that of internal atmospheric dynamics increases towards higher latitudes (Zwiers and Kharin 1998). The interannual SST variability over the extratropical oceans is strongly regulated by variations in the atmospheric circulation, whereas the ocean's effect on the

---

**Electronic supplementary material** The online version of this article (<https://doi.org/10.1007/s00382-018-4306-0>) contains supplementary material, which is available to authorized users.

---

✉ Jouni Räisänen  
jouni.raisanen@helsinki.fi

<sup>1</sup> Institute for Atmospheric and Earth System Research/  
Physics, Faculty of Science, University of Helsinki, P.O.  
Box 64, 00014 Helsinki, Finland

extratropical atmosphere is more subtle (Bjerknes 1964; Deser and Blackmon 1993). Nevertheless, there is evidence that the ocean plays a more active role in generating atmospheric variability on decadal than interannual time scales (Kushnir 1994).

Although ultimately driven by atmospheric and oceanic circulation, variations in near-surface temperature are modulated by feedbacks that affect the atmospheric and surface energy budget. For example, both reduced cloudiness (which increases the absorption of solar radiation) and reduced soil moisture (which decreases the evaporative cooling of the surface) have been identified as important ingredients in European heat waves (Black et al. 2004; Fischer et al. 2007). Consistent with both mechanisms, the correlation between monthly temperature and precipitation is widely negative over midlatitude continents in summer and in tropical land areas (Trenberth and Shea 2005). As another example, Park et al. (2015) used the climate feedback—response analysis method (Lu and Cai 2009) to explain the temperature differences between winters with a strong and a weak Siberian high. They found that lower temperatures in central Siberia in winters with a strong Siberian high result from a combination of factors, including cold advection, increased surface cooling due to larger sensible heat flux, and weaker greenhouse effect due to reduced water vapour and cloud water content. Hu et al. (2016) used the same method to energetically explain the different distribution of surface temperature anomalies in Eastern and Central Pacific El Niños. Although the heat flux from the ocean was identified as the main cause of surface temperature anomalies in both cases, the larger warming in the Eastern Pacific during the Eastern Pacific El Niños was attributed to a stronger water vapour feedback in this area.

Despite the previous work, a systematic view on the energetics of interannual temperature variability still appears to be lacking. Variations in several factors, among others atmospheric energy transport, surface-atmosphere energy exchange, surface albedo, clouds, and the atmospheric clear-sky greenhouse effect might all be important under at least some circumstances. But how important are they in general, in different parts of the world and in different seasons? This study aims to give at least an initial answer to this question, focusing on the interannual variability of monthly mean temperatures. The study is based on data sets from two modern atmospheric reanalyses (Sect. 2) and an energy balance framework that was earlier used for analysis of model-simulated CO<sub>2</sub>-induced temperature changes by Räisänen (2017; hereafter R17) (Sect. 3). The results are reported in Sect. 4, and some aspects of their physical interpretation are discussed further in Sect. 5. The main conclusions are presented in Sect. 6.

## 2 Data sets

Data from the ERA-Interim (Dee et al. 2011) and MERRA2 (Gelaro et al. 2017) reanalyses for the years 1980–2016 are used. The variables required by the energy balance decomposition include surface air temperature, total cloudiness, surface latent and sensible heat fluxes, and surface and top-of-the-atmosphere (TOA) downward and upward short-wave (SW) and long-wave (LW) radiative fluxes for both all-sky and clear-sky conditions (Table 1 in R17). These variables were downloaded as monthly means in a 2.5° × 2.5° latitude–longitude grid.

For ERA-Interim, surface pressure and six atmospheric variables ( $u$  and  $v$  wind, vertical velocity  $\omega$ , temperature, geopotential and specific humidity) at 37 pressure levels were additionally downloaded at 0.75° × 0.75° horizontal resolution and 6-h time interval. This large (2.8 TB) data set was used for explicit calculation of the atmospheric energy flux convergence term (Sects. 3.2, 4.5 and Appendix A) that was inferred as a residual in the other parts of the analysis.

The suitability of reanalysis data sets for energy budget analysis might be questioned because reanalyses violate energy conservation (e.g., Trenberth and Fasullo 2013) and show spurious large-scale trends associated with changes in the observing system (Allan et al. 2014). However, because the focus in this study is on interannual climate variability, the energy budget biases only matter to the extent that they vary from year to year. We assessed this issue in two ways, by analyzing the analysis increments in MERRA2 and by studying the mutual agreement and differences between ERA-Interim and MERRA2. The analysis increments were found to be large, but their impact on our main diagnostic results is moderated by their relatively weak correlation with the actual temperature anomalies (Section S1 in the Supplementary material). Furthermore, ERA-Interim and MERRA2 give a largely consistent view on the energetics of interannual temperature variability, although there are

**Table 1** Correlation of  $\Delta T$  and its main energy balance components between the ERA-Interim and MERRA2 reanalyses

	IAV	SD	SDC
$\Delta T$	0.92	0.98	0.98
$LW_{CLEAR}$	0.91	0.90	0.86
$SW_{CLEAR-ATM}$	0.24	0.29	0.43
$SW_{ALBEDO}$	0.72	0.86	0.72
$CLOUD$	0.57	0.70	0.56
$SURF$	0.85	0.96	0.90
$CONV$	0.88	0.97	0.92

IAV = spatiotemporal correlation of interannual variability (37 years × 12 months × global area); SD and SDC: the correlation of the SDs and SDCs (12 months × global area)

in many cases substantial quantitative differences between these two reanalyses (Sect. 4.1).

### 3 Methods

This section first describes the main features of the R17 energy balance method and its application to the interannual variability of monthly mean temperatures. After this, the methods used in the explicit calculation of atmospheric energy flux convergence in the ERA-Interim reanalysis are summarized. They are described in more detail in Appendix A.

#### 3.1 Energy balance framework

The R17 method is built around the concept of effective planetary emissivity  $\epsilon_{eff}$ , which connects the surface air temperature  $T$  to the outgoing longwave (LW) radiation  $L$  at the TOA

$$L = \epsilon_{eff} \sigma T^4 \tag{1}$$

and is (in broad terms, see Sect. 4.4) an inverse measure of the atmospheric greenhouse effect. Thus, warm anomalies in  $T$  require either a negative anomaly in  $\epsilon_{eff}$ , a positive anomaly in  $L$ , or both. Combining (1) with the atmospheric energy budget equation gives

$$\epsilon_{eff} \sigma T^4 = S - G + \left( C - \frac{\partial E}{\partial t} \right) \tag{2}$$

where  $S$  is net SW radiation at the TOA,  $G$  net downward heat flux to the surface,  $C$  horizontal energy flux convergence in the atmosphere, and  $E$  the total energy in the atmospheric column.

Referring to the climatological monthly mean of variable  $X$  as  $X_{CLIM}$ , the anomaly is  $\Delta X = X - X_{CLIM}$ . After also defining  $[X] = (X + X_{CLIM})/2$ , (2) leads to

$$\sigma [\epsilon_{eff}] \Delta(T^4) = \underbrace{-\sigma \Delta \epsilon_{eff} [T^4]}_I + \underbrace{\Delta S}_{II} \underbrace{-\Delta G}_{III} + \underbrace{\Delta \left( C - \frac{\partial E}{\partial t} \right)}_{IV} \tag{3}$$

Finally, linearizing the left side of (3) as

$$\sigma [\epsilon_{eff}] \Delta(T^4) \approx 4\sigma [\epsilon_{eff}] [T]^3 \Delta T = D \Delta T \tag{4}$$

allows one to decompose the temperature anomaly  $\Delta T$  as

$$\Delta T = \underbrace{LW}_I + \underbrace{SW}_{II} + \underbrace{SURF}_{III} + \underbrace{CONV}_{IV} + ERR \tag{5}$$

where the terms I–IV in (3) have been divided by  $D = 4\sigma [\epsilon_{eff}] [T]^3$ . These four terms represent the temperature

anomalies due to LW and SW radiation, net surface energy flux, and atmospheric energy flux convergence minus storage. On the average,  $D \approx 3.3 \text{ Wm}^{-2} \text{ K}^{-1}$ , so that a  $1 \text{ Wm}^{-2}$  energy perturbation is typically equivalent to 0.3 K in temperature.

The linearization in (3) is performed around  $(T + T_{CLIM})/2$  rather than  $T_{CLIM}$ . This makes the linearization residual  $ERR$  very small, with a mean absolute value of less than  $10^{-3}$  K. On the other hand, variations in  $D$  allow the means of  $LW$ ,  $SW$ ,  $SURF$  and  $CONV$  to differ from zero when averaged over the whole period. Nevertheless, their mean values are small relative to their interannual variability that is the focus of this paper.

The terms  $LW$  and  $SW$  are further divided to two and five parts, respectively

$$LW = LW_{CLEAR} + LW_{CRE} \tag{6}$$

$$SW = SW_{IN} + SW_{CLEAR-ATM} + SW_{ALBEDO} + SW_{CLOUD} + SW_{NL} \tag{7}$$

In (6),  $LW_{CLEAR}$  is the temperature anomaly attributed to the clear-sky greenhouse effect (anomaly of  $\epsilon_{eff}$  under clear-sky conditions) and  $LW_{CRE}$  that due to the long-wave cloud radiative effect. The division (7) is based on the approximate partial radiative perturbation (APRP) method (Taylor et al. 2007). The five terms represent the SW radiation anomalies associated with incoming SW radiation ( $SW_{IN}$ ), SW radiative properties of the clear-sky atmosphere ( $SW_{CLEAR-ATM}$ ), surface albedo ( $SW_{ALBEDO}$ ), clouds ( $SW_{CLOUD}$ ), and nonlinear effects ( $SW_{NL}$ ). Different notations are used for the two cloud terms ( $LW_{CRE}$  and  $SW_{CLOUD}$ ) because of the difference in their way of calculation.  $LW_{CRE}$  is based directly on the anomaly in the cloud radiative effect, which may be affected by variations in the clear-sky radiative properties of the atmosphere in addition to those in clouds. By contrast,  $SW_{CLOUD}$  attempts to isolate the effect of cloud anomalies on the SW radiation budget by explicit although highly simplified modelling of the radiative transfer. For further details, see R17.

The focus in this paper is on interannual variability. To separate this from long-term climate change, all the anomalies were linearly detrended before the energy budget decomposition. Conversely,  $X_{CLIM}$  as given above Eq. (3) was defined by the least-square trend line fitted for each calendar month separately.

#### 3.2 Direct calculation of the convergence term

For most parts of the analysis,  $CONV$  in (5) was calculated from the difference of the net surface and TOA energy fluxes. This is straightforward but offers no information on the mechanisms that contribute to  $CONV$ . Therefore, we also estimated  $CONV$  directly from ERA-Interim data. In

practice, the calculation of energy flux convergence was replaced by calculation of three-dimensional energy advection in the interest of numerical accuracy (Appendix A). However, because the convergence and advection forms are physically equivalent, the word “convergence” will be used when discussing the results.

The resulting direct estimate for  $CONV$  is

$$CONV_{DIR} = CONV_{MON} + CONV_{SM} + STOR \quad (8)$$

Here  $CONV_{MON}$  denotes the temperature anomaly attributed to the energy flux convergence by the monthly mean flow, whereas  $CONV_{SM}$  results from sub-monthly covariation between winds and atmospheric energy content.  $STOR$  represents the change in the total atmospheric energy content, being positive when the energy content anomaly decreases from the beginning to the end of the month (term IV in (3)).

## 4 Results

To introduce the method, Fig. 1 depicts time series of January and July mean temperature anomalies in central Finland (62.5°N, 25°E) and their decomposition to the main energy budget contributions, separately for the two reanalyses. Temperature variability at this location is much larger in January than July (standard deviation ~4 vs. ~1.5 °C), and the energy contributions to the variability are also partly different. In January,  $LW_{CLEAR}$ ,  $CONV$  and to a slightly smaller extent  $CLOUD$  are the main drivers of variability, with positive values in most of the mild Januarys and negative values in

most of the cold Januarys.  $LW_{CLEAR}$  and  $CLOUD$  also act to amplify temperature variability in July, but  $CLOUD$  is more important than  $LW_{CLEAR}$  particularly in ERA-Interim. By contrast,  $CONV$  mostly opposes the actual temperature anomalies in July. The same applies to  $SURF$  in both January and July, since the anomalous net surface energy flux is directed from the atmosphere to the ground in most anomalously warm months and vice versa in anomalously cold months.

$SW_{ALBEDO}$  is excluded from Fig. 1 because it is negligible in both January (due to lack of solar radiation) and July (when the surface is always snow-free).  $SW_{CLEAR-ATM}$  is also generally small, but is substantially negative in MERRA2 after the Mt. Pinatubo eruption in July 1992 and 1993 (Fig. 1d). This feature is lacking from ERA-Interim, which uses prescribed climatological aerosol distributions that vary seasonally but not from year to year, and thus excludes the Pinatubo eruption (Dee et al. 2011; Allan et al. 2014). In MERRA2, by contrast, aerosols are simulated explicitly based on emissions that vary from year to year, and observations of aerosol optical depth are assimilated into the analysis (Randles et al. 2017).

The time series from the two reanalyses agree well on the interannual temperature variations. Apart from  $SW_{CLEAR-ATM}$ , the same qualitatively applies to the energy balance contributors to this variability. However, quantitative differences are apparent. For example, in some Julys  $CLOUD$  and  $CONV$  differ by several °C between ERA-Interim and MERRA2, but to opposite directions. Recall that  $CONV$  is derived from the difference of the surface and TOA net energy fluxes and

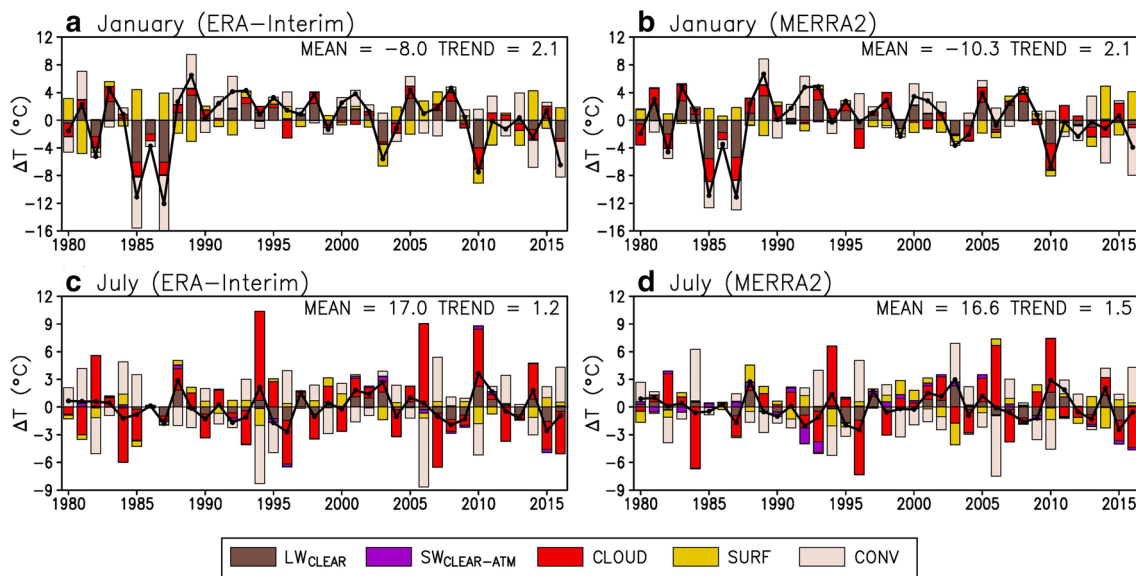


**Fig. 1** Linearly detrended temperature anomalies in central Finland (62.5°N, 25°E) in January and July 1980–2016 (solid lines) and the contributions of individual energy balance terms to them (bars, leg-

end at the bottom). For reference, the mean and the 36-year linear trend of temperature are given in the top-right corner of the figure panels



any reanalysis-specific errors in these fluxes are therefore directly mirrored in it.

### 4.1 Magnitude of the terms and the agreement between the two reanalyses

The global importance of the energy balance components is characterized in Fig. 2 with two statistical measures: (1) their interannual standard deviation, and (2) their contribution to the interannual standard deviation of temperature. The latter is calculated as.

$$SDC(i) = r(i)SD(i) \tag{9}$$

where  $SD(i)$  is the standard deviation of term  $i$  and  $r(i)$  is the correlation between term  $i$  and temperature. Using the definition of correlation, one can show that the  $SDCs$  sum up to the interannual standard deviation of temperature:

$$\sum_i SDC(i) = SD(\Delta T) \tag{10}$$

For Fig. 2, both the  $SDs$  and  $SDCs$  were first calculated for each month and grid box and then averaged over the 12 months and the global area, so to characterize the general behaviour of the terms.  $SW_{IN}$  and  $SW_{NL}$  are both very small, with  $SD < 0.1$  K, and will therefore not be discussed further. Conversely,  $SURF$  and  $CONV$  are very large, with  $SD \approx 5$  K. However, as discussed in Sect. 4.2, they turn out to have a strong mutual cancellation particularly over the oceans.  $LW_{CRE}$  and  $SW_{CLOUD}$  are also large,  $SW_{CLOUD}$  being the larger. Unsurprisingly, however, there is also

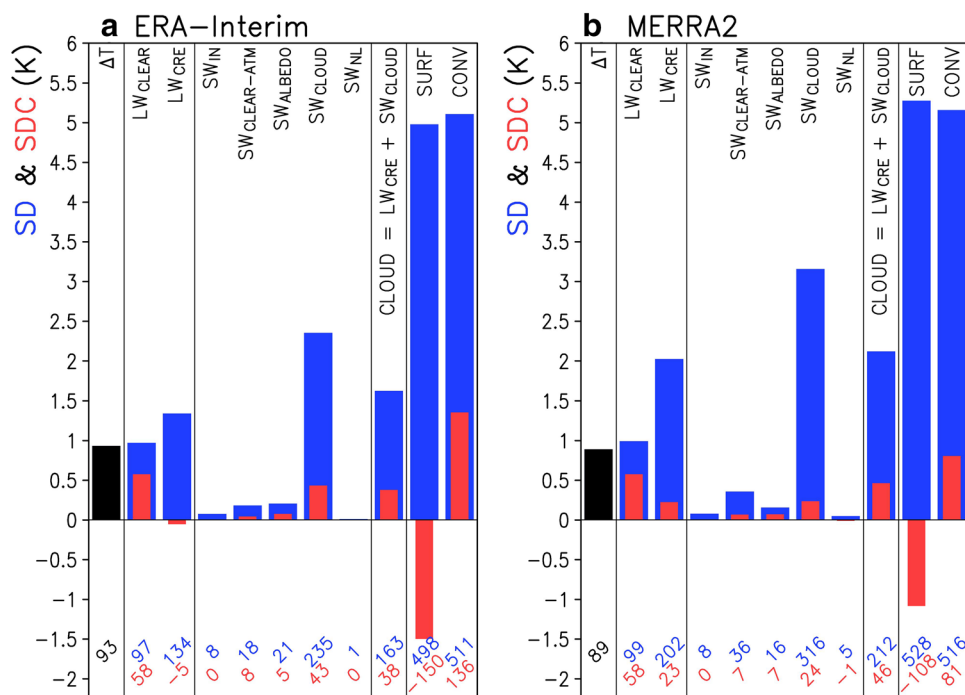
some compensation between  $LW_{CRE}$  and  $SW_{CLOUD}$ . We will therefore mainly study their sum, denoted as  $CLOUD$ , in the rest of this paper. Although smaller than  $SD(SW_{CLOUD})$ ,  $SD(CLOUD)$  is also substantial (9th column of Fig. 2a, b). Of the remaining terms,  $LW_{CLEAR}$  is of similar magnitude with the actual monthly mean temperature anomalies, whereas  $SW_{CLEAR-ATM}$  and  $SW_{ALBEDO}$  are relatively small on the average.

The largest average contributors to the standard deviation of  $\Delta T$  are, in this order,  $CONV$ ,  $LW_{CLEAR}$  and  $CLOUD$  (red bars in Fig. 2). The average  $SDCs$  of  $LW_{CRE}$  and  $SW_{CLOUD}$  are both positive in MERRA2 but the former is slightly negative in ERA-Interim. On the other hand, the net surface heat flux ( $SURF$ ) has a strong tendency to reduce interannual temperature variability. This is particularly the case over the extratropical oceans (Sect. 4.2).

The globally averaged  $SDs$  and  $SDCs$  are generally similar between the two reanalyses. The largest differences occur in the  $SD$  and  $SDC$  of  $CLOUD$  and its two components,  $SDC(SURF)$  and  $SDC(CONV)$  (recall that  $CONV$  is a residual). In addition,  $SD(SW_{CLEAR-ATM})$  is twice as large in MERRA2 than in ERA-Interim. This is consistent with the already mentioned difference in the treatment of aerosols.

To further quantify the agreement between ERA-Interim and MERRA2, the correlation coefficients between the two reanalyses were calculated for (1) the full space–time interannual variability of  $\Delta T$  and its energy balance components during the 37-year period, and the space–time variability in the (2)  $SDs$  and (3)  $SDCs$  over the global area and the 12 calendar months (Table 1). All three correlations are strongly

**Fig. 2** Typical magnitudes of the terms in Eqs. (5)–(7) in the ERA-Interim and MERRA2 reanalyses. The first column shows the interannual standard deviation ( $SD$ ) of monthly temperature anomalies ( $\Delta T$ ) averaged over the 12 months and the global area. The remaining columns show the corresponding  $SDs$  of the energy balance terms (blue) and their contribution to the standard deviation of  $\Delta T$  ( $SDC$ , red). The numeric values at the bottom give the  $SDs$  (upper) and  $SDCs$  (lower) in units of 0.01 K



positive for  $\Delta T$  ( $> 0.9$ ) and most of the major energy balance components, particularly  $LW_{CLEAR}$ ,  $SURF$  and  $CONV$  ( $\geq 0.85$ ). However, the correlations for  $CLOUD$  are somewhat lower, and the difference in the treatment of aerosols strongly deteriorates the agreement on  $SW_{CLEAR-ATM}$ . Maps of the inter-reanalysis differences in the SDCs are shown in Fig. S2. Typically, the differences on the grid box scale are about 10% of the two-reanalysis mean for the temperature anomalies, 25% for  $LW_{CLEAR}$ , of the order of 40% for  $SURF$  and  $CONV$ , and between 60 and 100% for  $SW_{CLEAR-ATM}$ ,  $SW_{ALBEDO}$  and  $CLOUD$ .

It seems obvious that MERRA2 provides more realistic estimates of  $SW_{CLEAR-ATM}$  than ERA-Interim. For the other terms, the relative performance of the two reanalyses is more difficult to assess, although some insight might be gained from comparison with satellite data (e.g., Loeb et al. 2018) and other observational data sets. In the figures shown in the rest of this paper, we will simply average the statistics derived from the two reanalyses to emphasize their common features. Selected maps for ERA-Interim and MERRA2 separately are included in the Supplementary material (Figs. S3, S4, S6, S7 and S12, S13).

## 4.2 Geographic variability

The first column in Fig. 3 shows the SDs of  $\Delta T$  and its main energy balance components, averaged over the 12 months and the two reanalyses. The corresponding SDCs are displayed in the third column, with the grey shading indicating areas where their sign is not robust. The SDC is considered robust if it has the same sign in the two reanalyses, and differs in at least one of them from zero at the 5% significance level based on a two-sided sign test (Appendix B). The SDs and SDCs are connected by the correlation between the individual energy balance terms and temperature, shown in the middle column. Following (9), the “average” correlation is defined here by dividing the average SDC by the average SD.

Interannual temperature variability is generally larger at high than low latitudes and over the continents than over the oceans (Fig. 3a). However, the Arctic Ocean and, relative to its latitude, the tropical East Pacific also stand out with large variability. The SD patterns for the individual energy balance components are variable (left column of Fig. 3). For example,  $SD(SW_{ALBEDO})$  is small in most areas, but locally large where interannual variations in sea ice and snow cover are substantial: the margins of the Arctic Ocean, off the coast of Antarctica, and in the Northern Hemisphere extratropical continents, notably the Tibetan Plateau (Fig. 3h). By contrast,  $SD(CLOUD)$  is large (1–4 K) nearly everywhere, but smaller over the Arctic Ocean, Greenland, Antarctica, and the deserts extending from Sahara to central Asia (Fig. 3k). An inspection of  $LW_{CRE}$  and  $SW_{CLOUD}$  separately (Fig. S5) suggests two main explanations for the relatively small

magnitude of  $SD(CLOUD)$  in these areas: lack of optically thick clouds (over deserts and ice sheets), and/or limited sensitivity of the TOA radiation balance to clouds where modest insolation (in polar regions in most of the year) and/or high surface albedo (over ice sheets and sea ice) make it easier for  $LW_{CRE}$  to offset  $SW_{CLOUD}$ .

$SD(SURF)$  and  $SD(CONV)$  are both very large over the oceans (Fig. 3n, q), exceeding 8 K in many areas mainly in the extratropics. Their patterns are very similar, which results from a strong mutual compensation. This compensation reflects, on one hand, the ability of the ocean to absorb large amounts of heat with only modest changes in the surface temperature, and on the other hand, the tendency of the atmospheric circulation to horizontally spread the effects of local energy input over a larger area (Sect. 5).  $SD(CONV)$  is also large over the continents, generally in the range 1–4 K, with the largest values at mid-to-high latitudes. By contrast,  $SD(SURF)$  is  $< 1$  K in most land areas, due to the modest heat capacity of the land surface. The main exception are the northern parts of Eurasia and North America, where variations in the energy consumed by snowmelt amplify the variability in the net surface heat flux in winter and spring.

How much a given energy term amplifies or attenuates temperature variability is affected by both its standard deviation and its correlation with temperature anomalies (Eq. (9)). A case in point is  $LW_{CLEAR}$ , which has a strong positive correlation ( $> 0.7$ ) with  $\Delta T$  in most extratropical areas, but a weaker or locally negative correlation with  $\Delta T$  in much of the tropics (Fig. 3c). This makes  $SDC(LW_{CLEAR})$  less positive in most of the tropics than at higher latitudes (Fig. 3d), although  $SD(LW_{CLEAR})$  is also large in the tropics (Fig. 3b). An exception with large  $SDC(LW_{CLEAR})$  is the equatorial East Pacific, where  $LW_{CLEAR}$  is both highly variable and highly correlated with temperature. The interpretation of  $LW_{CLEAR}$  is discussed in more detail in Sect. 4.4.

$SW_{CLEAR-ATM}$  is positively correlated with  $\Delta T$  in most regions, particularly at mid-to-high latitudes (Fig. 3f). This indicates a positive SW water vapor feedback due to a positive correlation between temperature and atmospheric water vapor, which leads to larger water vapor absorption of SW radiation in months with positive temperature anomalies. However, since  $SD(SW_{CLEAR-ATM})$  is relatively small, this term makes a fairly modest contribution to interannual temperature variability (Fig. 3e, g).

Where  $SD(SW_{ALBEDO})$  is substantial, this term is positively correlated with  $\Delta T$ , because warm anomalies typically coincide with negative anomalies in snow and ice cover (Fig. 3h, i). However, there are also areas where this correlation is negative. In particular, the negative correlation over Antarctica reflects a positive correlation between temperature and snowfall: higher snowfall during anomalously warm summer months counteracts the ageing of snow, thereby slightly increasing the surface albedo (Picard et al.



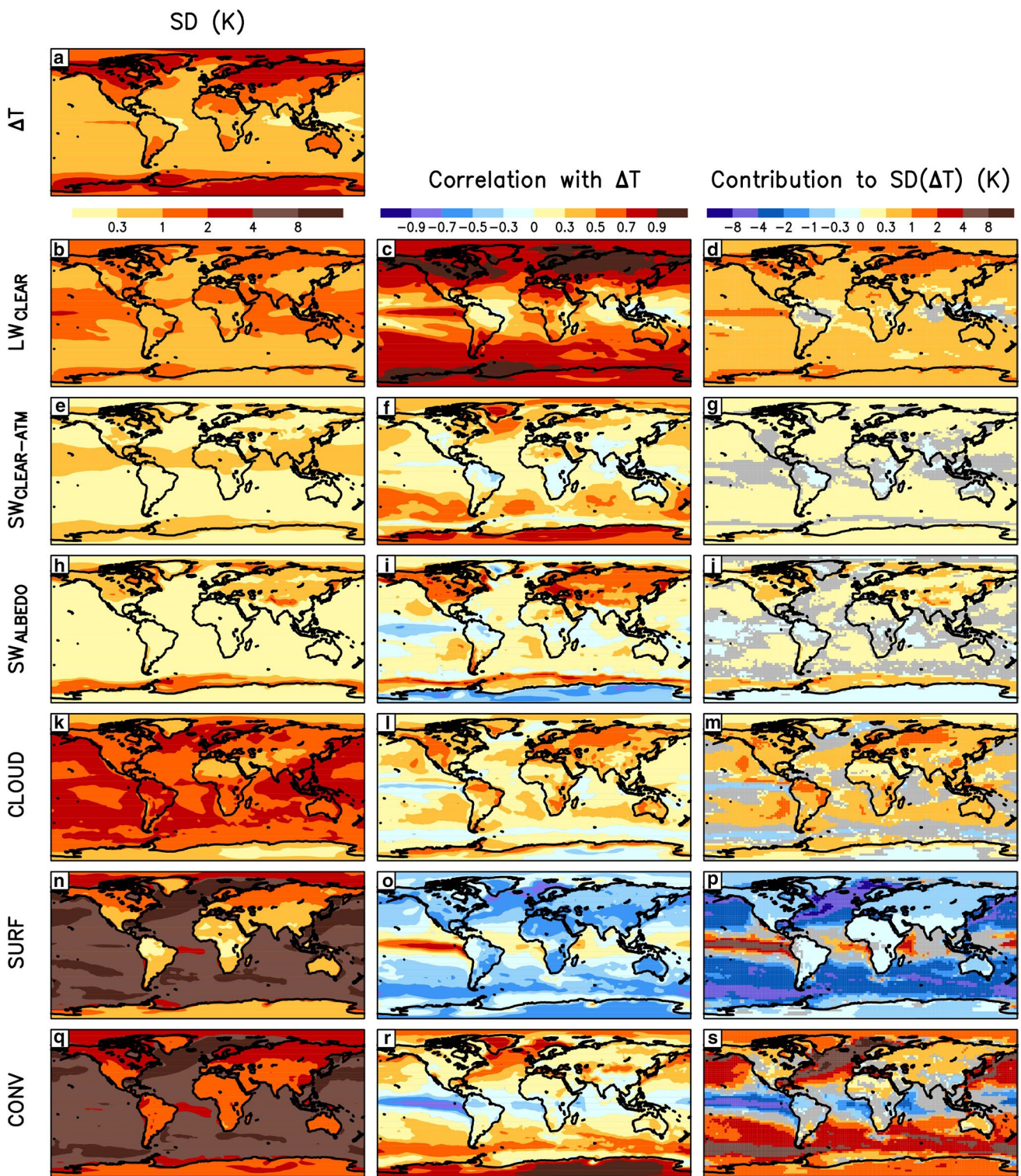


**Fig. 3** Left: interannual standard deviation of monthly mean temperature anomalies ( $\Delta T$ ) and their main energy balance components. Middle: Correlation between the individual energy balance components and  $\Delta T$ . Right: Contributions of the individual energy balance com-

ponents to the standard deviation of  $\Delta T$ . All statistics are averaged between ERA-Interim and MERRA2. In the third column, grey colour indicates areas where the sign of the standard deviation contribution is not robust (see Sect. 4.2 for definition)

2012). This feature is more pronounced in ERA-Interim than in MERRA2 (Figs. S3, S4).

*CLOUD* is also positively correlated with  $\Delta T$  in most areas, and therefore generally acts to amplify temperature variability (Fig. 3l, m). Exceptions with a slightly negative correlation include, among others, eastern tropical Pacific and parts of the Southern Ocean. The physical interpretation of *CLOUD* is discussed in some more detail in Sect. 4.3.

*SURF* and *CONV* strongly oppose each other over the oceans. In the tropics, particularly over the equatorial East Pacific, *SURF* is large in magnitude and positively correlated with  $\Delta T$ , and is thus strongly driving anomalies in surface air temperature (Fig. 3o, p). However, in the same areas, *CONV* strongly damps the temperature variability, effectively diffusing out the impact of the local surface heat flux anomalies (Fig. 3r, s). Over most of the mid-to-high-latitude oceans, the roles of *SURF* and *CONV* are reversed, with the atmospheric heat convergence strongly driving but the net surface heat flux strongly attenuating the temperature variability. This picture of mainly ocean-driven temperature variability over the tropical and atmosphere-driven variability over the extratropical oceans is consistent with a large number of earlier studies (e.g., Bjerknes 1964; Deser and Blackmon 1993; Wu and Kirtman 2007).

Over nearly all land areas, the variation in the net surface heat flux acts to reduce the interannual temperature variability (Fig. 3o, p). This effect is modest but not negligible: as averaged over the 12 months and all land,  $SDC(SURF) = -0.44$  K, or 30% of the corresponding mean of  $SD(\Delta T) = 1.47$  K. Conversely,  $SDC(CONV)$  is positive over most land areas (Fig. 3s). The correlation between *CONV* and  $\Delta T$  is mostly not very strong (Fig. 3r), but exceeds 0.7 over large parts of the Greenland and Antarctic ice sheets and 0.9 over East Antarctica. The high correlations in Greenland and Antarctica seem to be linked to the relatively modest interannual variability in the other energy balance terms over these ice sheets (left column of Fig. 3). On the other hand, *CONV* attenuates interannual temperature variability in northern South America and some other low-to-midlatitude land areas. The physical interpretation of *CONV* is explored in more depth in Sect. 4.5.

### 4.3 Seasonality

We next discuss the seasonality of the six main energy terms included in Fig. 3, focussing on their SDCs. Comparison between extended Northern Hemisphere winter (November-to-March, NDJFM) and summer (May-to-September, MJJAS) seasons reveals several differences (Fig. 4).

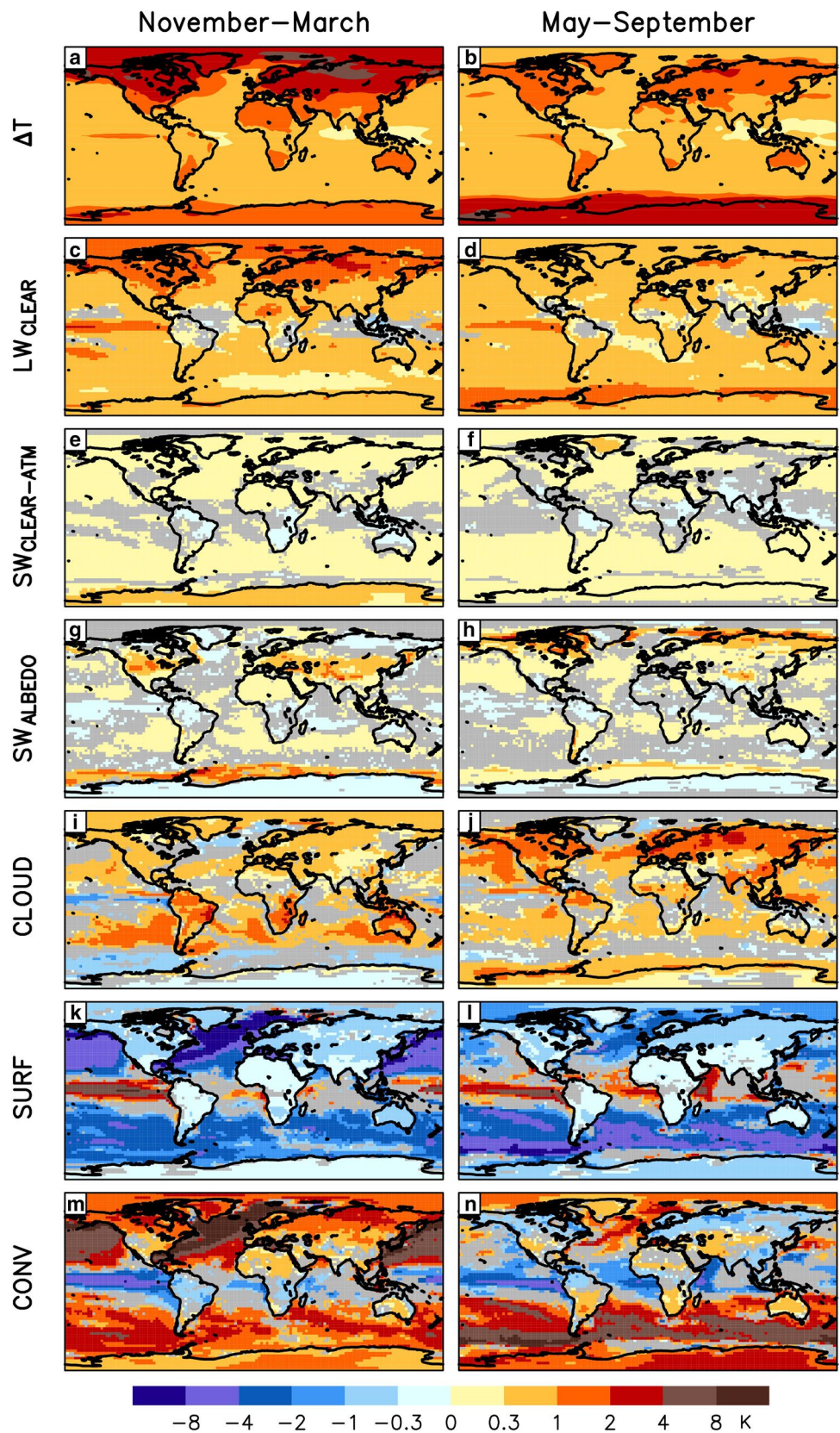
1. Temperature variability in extratropical latitudes is larger in the local winter than the summer season (Fig. 4a, b). The same applies to  $SDC(LW_{CLEAR})$  (Fig. 4c, d).
2.  $SDC(SW_{CLEAR-ATM})$  is largest over the summer hemisphere ice sheets, in Greenland in NDJFM and in Antarctica in MJJAS (Fig. 4e, f).
3. The seasonality of  $SW_{ALBEDO}$  reflects the seasonalities of snow and ice cover and incoming solar radiation. Accordingly, in the Northern Hemisphere continents,  $SW_{ALBEDO}$  is mainly important in midlatitudes in winter but in the Arctic in summer (Fig. 4g, h). Near the sea ice edge,  $SW_{ALBEDO}$  is mainly important during the local summer.
4.  $SDC(CLOUD)$  is typically more positive during the local summer than winter (Fig. 4i, j), particularly in the midlatitudes. This is due to  $SW_{CLOUD}$ , which strongly amplifies the temperature variability in the midlatitudes in summer, when solar radiation is abundant and reduced cloudiness therefore tends to increase temperature (Fig. S8). In winter, the paucity of solar radiation makes  $SW_{CLOUD}$  much less important. However,  $LW_{CRE}$  also plays a role, attenuating temperature variability when and where temperature is negatively correlated with (particularly high-top) cloudiness, but amplifying the variability when the correlation is positive. The latter is typical at mid-to-high latitudes in winter, as well as in the tropical East Pacific (Fig. S8). In the tropical East Pacific,  $SW_{CLOUD}$  and  $LW_{CRE}$  nearly cancel out (see also Fig. S10d), but in high latitudes in winter,  $LW_{CRE}$  dominates. Over the Arctic Ocean, the high-latitude Southern Ocean, and the Greenland and Antarctic ice sheets, the net effect represented by  $SDC(CLOUD)$  in Fig. 4i, j is therefore more positive in winter than in summer.
5. Reflecting the more vigorous extratropical atmospheric circulation and the stronger climatological temperature gradients in the winter hemisphere,  $SDC(CONV)$  is more positive and  $SDC(SURF)$  more negative over the mid-latitude oceans in winter than in summer (Fig. 4k–n). The seasonality of  $SDC(CONV)$  is even more striking over the northern halves of Eurasia and North America, where the atmospheric heat flux convergence strongly amplifies temperature variability in winter but slightly attenuates it in summer. The interpretation of *CONV* is explored further in Sect. 4.5.

As an example that illustrates the seasonal variation in more detail, the monthly contributions of the main energy balance terms to temperature variability in central Finland (cf. Fig. 1) are shown in Fig. 5. At this location, there is a gradual shift from large *CONV*- and  $LW_{CLEAR}$ -dominated variability in October–March to smaller *CLOUD*-dominated and *CONV*-suppressed variability in May–August.  $SW_{ALBEDO}$  only plays a significant role during the snowmelt season in March–April.

To explore the seasonal variation in another way, Fig. 6 identifies for every grid box and every second month of the



**Fig. 4** Interannual standard deviation of monthly mean temperature anomalies in **a** November–March and **b** May–September, and **c–n** the contributions of the main energy balance components to it. All statistics are averaged between ERA-Interim and MERRA2. Grey colour indicates areas where the sign of the standard definition contribution is not robust (see Sect. 4.2 for definition)





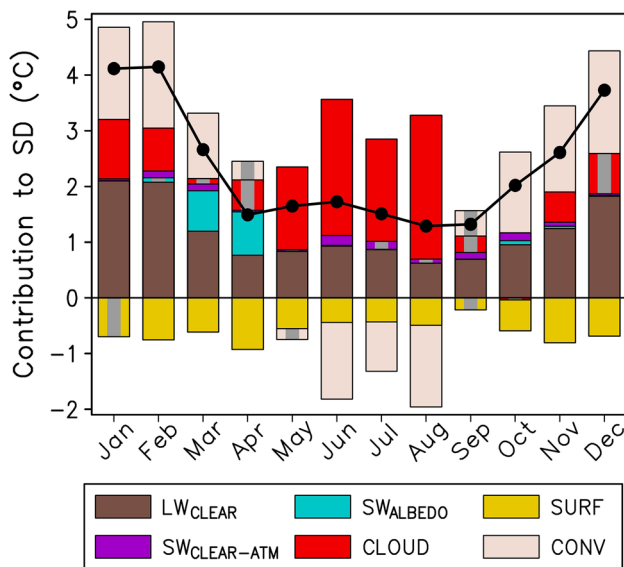


**Fig. 5** Interannual standard deviation of temperature in central Finland (the same grid box as in Fig. 1) (solid line) and the contributions of the six main energy balance terms to it (bars, legend at bottom; contributions that are not robust in the sense defined in Sect. 4.2 are indicated with a grey core)

year the term that provides the largest positive contribution to the standard deviation of temperature in this month. The broad picture over the oceans is seasonally uniform to the extent that *SURF* tends to make the largest contribution to interannual variability in the tropics and *CONV* at higher latitudes. However, the border between the *CONV*- and *SURF*-dominated zones is further poleward in summer than in winter, particularly in the Northern Hemisphere. *LW\_CLEAR* and *CLOUD* are also important, overriding all the other terms in some months in some ocean regions. *CLOUD* is more frequently the foremost term in summer than in winter; in particular it dominates the variability over large parts of the extratropical North Pacific and North Atlantic in summer. In addition to the larger insolation, this reflects the weaker midlatitude baroclinicity in summer, which reduces the importance of *CONV* relative to the winter season. To provide some more detail, diagrams similar to Fig. 5 are shown for six ocean grid boxes (in the Arctic Ocean, extratropical North Atlantic and North Pacific, eastern and western tropical Pacific, and high-latitude Southern Ocean) in Fig. S10.

Over most of the winter hemisphere continents, either *CONV* or *LW\_CLEAR* is the largest contributor to temperature variability. In summer, however, *CLOUD* is widely dominant in the extratropical continents. *CLOUD* is also commonly the largest term in tropical land areas, although this varies with month and region. Seasonal cycles of the individual energy terms in six land grid boxes (in Greenland, Siberia, Central Europe, the Tibetan Plateau, Amazonia and East Antarctica) are shown in Fig. S11.

The variations of snow and sea ice conditions make either *SW\_ALBEDO* or *SURF* the largest contributor to temperature variability in some months and locations. *SW\_ALBEDO* has this position in midwinter in parts of the United States and south-central Asia. During the spring, such areas shift northward. In May, in particular, *SW\_ALBEDO* is the largest term over much of northern Siberia and northernmost North America, as well as the Tibetan Plateau (see also Figs. S11b, d). Due to variations in the ice edge position, *SW\_ALBEDO* is also locally dominant over the Arctic and Antarctic Oceans in the local spring and summer (see also Figs. S10a, f). Variations in ice conditions also dramatically affect the atmosphere–ocean heat exchange during the cold season (Deser et al. 2010; Petrie et al. 2015). This locally makes *SURF* the largest contributor to temperature variability near the sea ice edge in late fall and winter, both over the Arctic Ocean and the high-latitude Southern Ocean (see also Figs. S10a, f).

Averaging over all 12 months and the global area, *CONV* is the largest contributor to variability in 47% of cases, followed by *CLOUD* (21%), *LW\_CLEAR* (16%), *SURF* (14%), and *SW\_ALBEDO* (2%). *SW\_CLEAR-ATM* only has this position in limited parts of the Antarctic continent in the local summer (0.1%).

To complement the overview provided this far, we next focus on the physical interpretation of two of the major energy terms: *LW\_CLEAR* (Sect. 4.4) and *CONV* (Sect. 4.5). In both cases, there are several factors involved and a more detailed analysis is therefore useful.

#### 4.4 Factors affecting *LW\_CLEAR*

Using the method detailed in Appendix C, the term *LW\_CLEAR* was further decomposed as

$$LW_{CLEAR} = LW_{CLEAR-S} + LW_{CLEAR-WW} + LW_{CLEAR-LR} + \epsilon \quad (11)$$

Here *LW\_CLEAR-S* represents variations in an effective surface emissivity calculated from the monthly means of surface air temperature and surface upward LW radiation (Eq. (21)). In practice, this term mainly reflects variations in the surface minus surface air temperature difference. The next two terms represent the main factors expected to affect the atmospheric clear-sky greenhouse effect (Webb et al. 1993), i.e. the atmospheric water vapor content (WW) and the lapse rate between the surface and the midtroposphere (LR). These terms were estimated using linear regression.  $\epsilon$  is the residual from this regression.

The factors that contribute to  $SDC(LW_{CLEAR})$  based on (11) are analysed in Fig. 7. Variations in the effective surface emissivity (term *LW\_CLEAR-S*) are unimportant over most land areas (Fig. 7a). However, they are more important over the mid-to-high latitude oceans, particularly the northern North Atlantic, where relatively large differences between

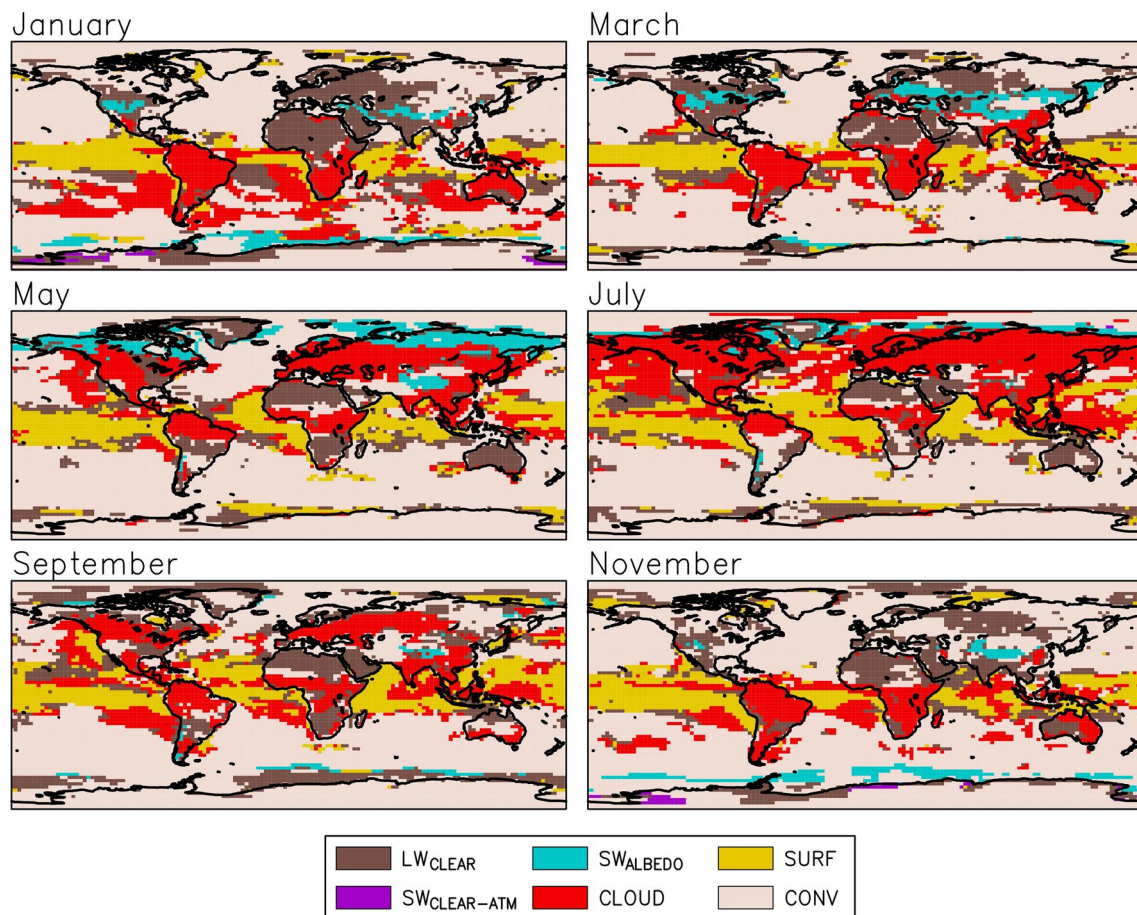


**Fig. 6** Largest contributors to interannual temperature variability in six calendar months, based on the mean of the ERA-Interim and MERRA2 results

the surface and surface air temperatures occur. Elsewhere,  $SDC(LW_{CLEAR})$  is dominated by variations in the atmospheric clear-sky greenhouse effect.

Both the water vapour and the lapse rate variations are found to amplify temperature variability in most areas (Fig. 7b, c). The lapse rate contribution (Fig. 7c) is largest in areas where temperature anomalies typically have a bottom-heavy structure, so that anomalies of surface temperature are not accompanied by equally large anomalies aloft. This is generally the case in high latitudes (especially in winter, Figs. S16, S17), but also over dry land areas such as Australia. The lapse rate contribution is also substantial in the easternmost tropical Pacific, where local SST variations mainly affect air temperature in the boundary layer below a climatological subsidence inversion (Andrews and Webb 2018). The water vapour contribution is widely dominant at lower latitudes, being particularly large over the central and eastern Pacific Ocean (Fig. 7b), but is still not positive everywhere. One of the exceptions is the western tropical Pacific, where the highest surface air temperatures coincide with remotely forced anomalous subsidence that warms the

surface by reducing cloud cover but also simultaneously reduces the atmospheric water vapour (Trenberth and Shea 2005).

#### 4.5 Interpretation of $CONV$

For the maps and diagrams shown this far,  $CONV$  was calculated as a residual. Here we report the results obtained from the direct calculation of the term using ERA-Interim data (Sect. 3.2 and Appendix A).

It is first necessary to note that  $CONV_{DIR}$  (8) and the residual  $CONV$  are far from identical.  $CONV_{DIR}$  exhibits larger interannual variability than  $CONV$  (Figs. S18a, d), and the interannual standard deviation of their mutual difference exceeds 4 K in many parts of the world (Fig. S18g). Given the earlier experience of numerical difficulties in the calculation of atmospheric energy flux convergence (e.g., Chiodo and Haimberger 2010; Mayer and Haimberger 2012; Liu et al. 2017), these differences are not unexpected. Nevertheless, the time series of  $CONV_{DIR}$  and  $CONV$  are positively correlated nearly everywhere, and over most of the oceans

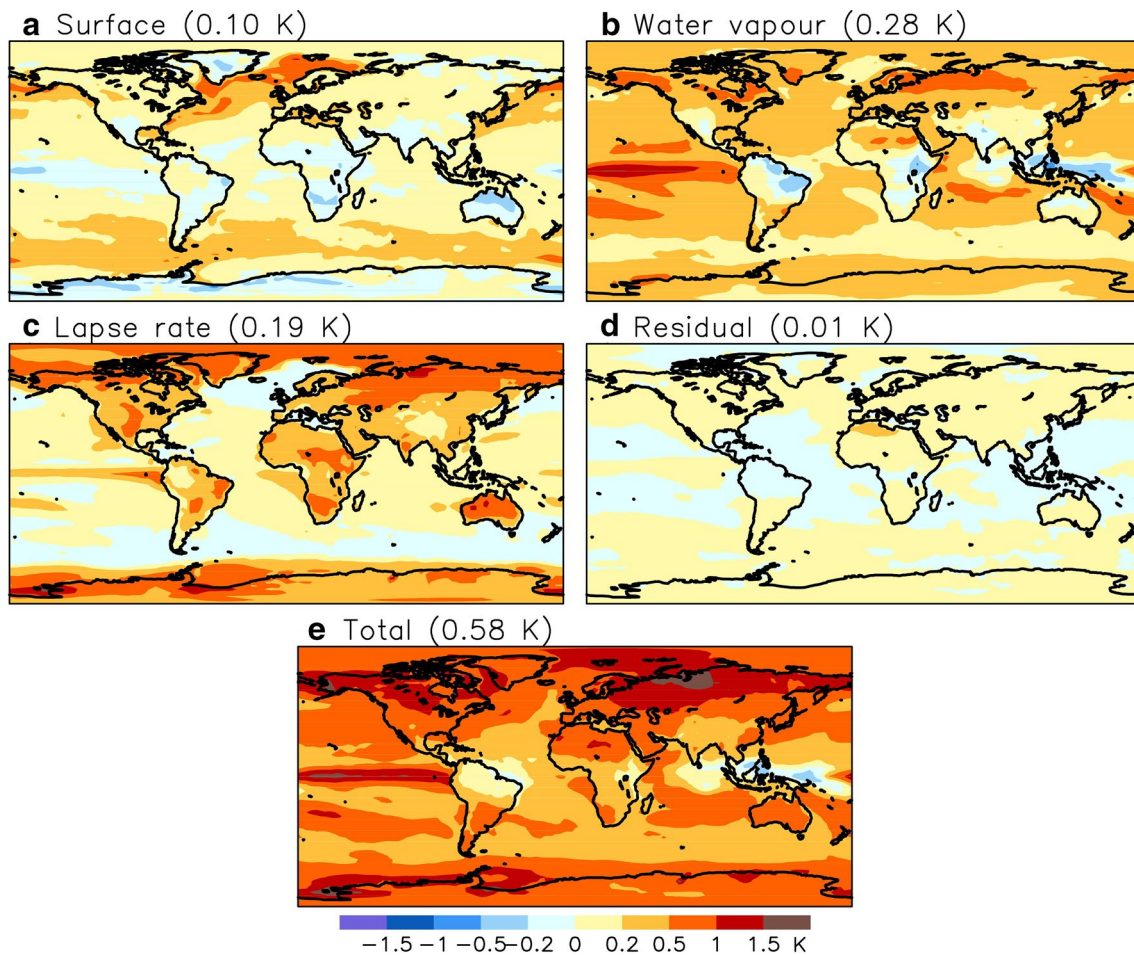


**Fig. 7** Division of  $SDC(LW_{CLEAR})$  (e) to contributions from the four terms in Eq. (11) (a–d). All values are averaged over the 12 months and between ERA-Interim and MERRA2. The global area means are given in the headings. Note that the colour scale differs from Figs. 3 and 4

the correlation exceeds 0.7 (Figure S19).  $CONV_{DIR}$  and  $CONV$  also share broadly the same statistical relationship with temperature anomalies, particularly over the oceans (Figs. S18b, c, e, f). Still, the SDC of the residual estimate tends to be somewhat more positive than that of the direct estimate over the midlatitude continents, and less positive over the midlatitude oceans (Fig. S18i). This systematic feature might reflect a mismatch between the interannual variations of the atmospheric energy flux convergence and the TOA and surface energy fluxes in ERA-Interim, rather than just numerical errors in  $CONV_{DIR}$ .

Following (8),  $CONV_{DIR}$  was divided into three terms that represent the energy flux convergence by the monthly mean atmospheric flow and sub-monthly variations in the flow, and changes in the atmospheric energy content during a month (“storage”) (Fig. 8). This division reveals a strong tendency of cancellation between the monthly mean and sub-monthly energy flux convergence components at extratropical latitudes (Fig. 8d–i). In midlatitudes, the monthly mean energy flux convergence component amplifies

temperature variability (Fig. 8e, f), whereas the sub-monthly component acts to reduce the variability (Fig. 8h, i) but is typically slightly smaller in magnitude. Outside of mid-latitudes, the situation is less clear-cut. For example, over parts of Antarctica, sub-monthly energy flux convergence appears to amplify, but monthly mean convergence to attenuate temperature anomalies. In the tropics, the monthly mean component generally dominates over the sub-monthly component. Finally, Fig. 8j shows that within-month changes in atmospheric energy storage are a non-negligible part of  $CONV$  in individual months. However, these changes neither systematically amplify nor reduce the temperature variability (Fig. 8l). The atmospheric energy content tends to be broadly in phase with surface air temperature, and hence its change from the beginning to the end of the month is nearly uncorrelated with the monthly mean temperature anomaly (Fig. 8k).

The tendency of sub-monthly energy flux convergence to reduce interannual temperature variability in midlatitudes is consistent with earlier research. In particular, Lau and



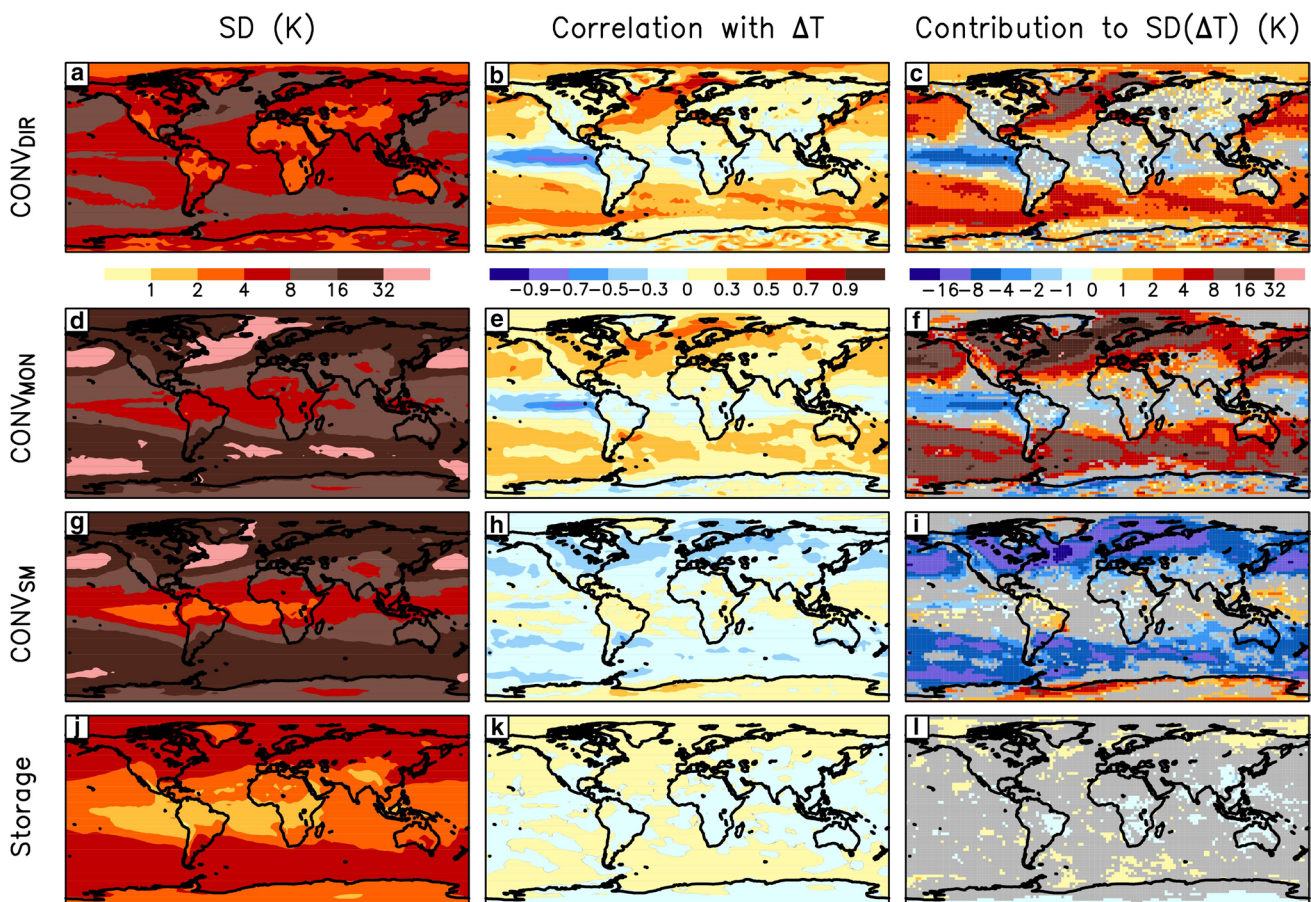


**Fig. 8** Term CONV as calculated directly from energy flux convergence and storage using ERA-Interim data (a–c), and its decomposition to the contributions of d–f the monthly mean flow, g–i sub-monthly flow variations and j–l atmospheric energy storage. The

three columns are the same as in Fig. 3. Grey colour indicates areas where the sign of the standard definition contribution is not significant at 5% level based on a sign test

Nath (1991) found a negative correlation between anomalies of monthly mean temperature at the 850 hPa level and the temperature tendencies induced by synoptic-scale eddy heat fluxes (their Fig. 13). This diffusion-like behavior of eddies also applies to the time mean flow, with the eddy heat fluxes acting to reduce both the meridional and zonal gradients of temperature (Lau and Holopainen 1984). One may therefore assume that, at least in the midlatitudes, the anomalies in the sub-monthly energy flux convergence are more a consequence than a cause of the monthly mean energy content (or temperature) anomalies.

Monthly mean energy flux convergence tends to amplify and its sub-monthly counterpart to attenuate the midlatitude temperature variability in both the NDJFM and MJJAS seasons (Fig. S20). Interestingly, however, the sub-monthly energy flux convergence makes a more negative SDC contribution in the northern parts of Eurasia and North America in summer than in winter. The tendency of CONV to amplify temperature variability in winter but to rather reduce it in summer in these areas (Fig. 4m, n) thus reflects a delicate

balance between the contributions of the monthly mean and sub-monthly energy convergence.

### 5 Discussion

The results of diagnostic techniques tend to become more difficult to interpret when the quantity of interest (here the temperature anomaly) is a small residual of large but compensating right-hand-side terms. The tendency of compensation between the monthly mean and sub-monthly energy flux convergences was already discussed in Sect. 4.5. Another equally important case is the compensation between CONV and SURF over the ice-free oceans.

As shown in R17,

$$\Delta(S - L) = \Delta G - \Delta\left(C - \frac{\partial E}{\partial t}\right) = -D(SURF + CONV) \tag{12}$$

The compensation between *SURF* and *CONV* therefore indicates that, over the ice-free oceans, the anomalies in the net TOA radiation flux  $S-L$  are smaller than those in the net surface energy flux  $G$ . In fact, the average interannual standard deviation of  $G$  as calculated over the 12 months and all ocean grid boxes exceeds the standard deviation of  $S-L$  by more than a factor of three (not shown). This difference is qualitatively explicable by the fact that the TOA radiation balance is much less sensitive to variations in air temperature than the net surface energy flux is to the air–sea temperature difference. Everything else being the same, a 1 K anomaly in  $T$  only increases  $L$ , and hence reduces  $S-L$ , by  $D\Delta T \approx 3.3 \text{ Wm}^{-2}$  (Eqs. (1) and (4)). On the other hand, bulk parameterizations of turbulent energy fluxes (e.g., Kara et al. 2000) indicate a change of up to several tens of  $\text{Wm}^{-2}$  in the net surface energy flux per each 1 K change in the air–sea temperature difference. Over the ice-free oceans, where a substantial net surface flux can be sustained by the heat capacity of the ocean mixed layer,  $\Delta G$  can thus easily exceed  $\Delta(S-L)$  even when the anomaly in the air–sea temperature difference is relatively small.

One may argue that the multiplier  $D^{-1} \approx 0.3 \text{ K W}^{-1} \text{ m}^2$  used in (5) exaggerates the actual sensitivity of surface air temperature to variations in local energy input. This is particularly the case over the ice-free ocean, due to the ability of the net surface flux to consume a large fraction of any anomalous energy input into the air column. However, the diffusive behavior of the sub-monthly atmospheric energy flux convergence (Sect. 4.5) implies that the same also applies in other areas. Anomalies in the energy input into an air column, regardless of whether they originate from the net surface energy flux, cloudiness or, for example, surface albedo, are only partly balanced by local temperature-mediated changes in the TOA radiation balance. A large fraction of the energy input anomaly rather tends to be exported away by the atmospheric circulation.

To alleviate the systematic compensations, an energy budget framework should ideally take into account the effects of surface air temperature anomalies on *SURF* and *CONV*, rather than treating all of *SURF* and *CONV* as independent right-hand-side terms. However, this would require a substantial extension of the method. First, the energy budgets of the upper ocean and ground should be explicitly included, in addition to that of the atmosphere (Hedemann et al. 2017; Liu et al. 2017). Second, the effect of temperature anomalies on atmospheric horizontal energy flux convergence should be parameterized as a diffusion process. The second requirement is particularly difficult to achieve in a single-column framework, because the energy flux convergence is regulated by the gradients rather than the absolute local values of temperature and atmospheric energy content.

A local and instantaneous energy budget framework cannot identify processes that are non-local in space or time.

For example, during an El Niño, atmospheric energy flux divergence over central and eastern tropical Pacific acts to cool the air locally, thereby balancing a large fraction of the anomalous net surface energy flux. However, energy flux divergence in one area requires convergence elsewhere. Due to the stationary Rossby waves excited by diabatic heating anomalies (Simmons 1982; Ji et al. 2016), this energy redistribution process is more complicated than just horizontal diffusion. As another example, an anomaly in atmospheric circulation in the preceding months might help to build a warm or cold anomaly in the upper ocean temperature in some area, which would then feed back to the atmosphere by inducing an anomalous net surface energy flux. Thus, although energy budget analysis is useful for diagnosing the origin of temperature anomalies, it alone will not reveal the full cause-effect chain of events.

## 6 Conclusions

This study has investigated the energetics of interannual temperature variability in the ERA-Interim and MERRA2 reanalyses. Using the method introduced in R17, the anomalies in monthly mean surface air temperature were decomposed to six main components, representing the variations in (1) the atmospheric clear-sky greenhouse effect, (2) clear-sky SW radiative properties of the atmosphere, (3) surface albedo, (4) clouds, (5) the net surface energy flux, and (6) atmospheric energy flux convergence minus storage. Based on their covariation with the actual temperature anomalies, the effects of these individual components on temperature variability were then statistically diagnosed. A rich variety in the energetics of temperature variability in different areas and times of the year was found, depending on the surface conditions, availability of solar radiation and the local meteorological characteristics. Nevertheless, the main findings are the following:

1. Over the ice-free oceans, anomalies in surface air temperature are typically a small residual of opposite contributions from the net surface heat flux and atmospheric energy flux convergence. In the tropics, particularly in the eastern Pacific, the net ocean-to-atmosphere heat flux provides the main energy source for temperature variability, but most of this energy input is transported away by the atmospheric circulation. This pattern is reversed at higher latitudes, where variations in atmospheric energy flux convergence are large but are mainly consumed by heating or cooling the water mass, rather than changing the surface air temperature.
2. The net surface heat flux also tends to attenuate temperature variability on land but is mostly a secondary term in the energy budget. Major energetic drivers of tempera-



ture variability over land include, depending on season and location, variations in the atmospheric energy flux convergence, clouds, the clear-sky greenhouse effect, and surface albedo. Nonetheless, atmospheric energy flux convergence reduces rather than amplifies temperature variability over large parts of Eurasia and North America in summer, partly compensating a strongly positive cloud contribution to temperature variability. The same happens in some tropical land areas, especially northern South America.

- Care is needed in the interpretation of atmospheric energy flux convergence, which is affected by variations in both the atmospheric circulation and the atmospheric energy content and hence temperature. Thinking of anomalies of energy flux convergence simply as a cause of temperature anomalies is therefore not justified. In midlatitudes, in particular, our results reveal a duality between time scales, with anomalies in the monthly mean flow amplifying, but the sub-monthly variations attenuating temperature variability via their effect on the energy flux convergence. The net of these two very large components leaves a much smaller residual, particularly over land. The counter-intuitive situation in which the net effect of the energy flux convergence is to reduce temperature variability may arise when other components in the energy balance strongly act to amplify the variability. This is the case, for example, with cloud anomalies in much of Eurasia and North America in summer. Thus, although this has not been directly addressed herein, many summer heatwaves with reduced cloudiness may actually coincide with anomalous energy transport out of the air column.

The two reanalyses agree well on these general features, but some quantitative differences are evident. The ERA-Interim minus MERRA2 differences in the individual terms typically range from about 25% to 100% of the two-reanalysis mean on the grid box scale. Perhaps unsurprisingly, the effect of clouds is one of the most uncertain terms in the decomposition.

By analyzing the energetic contributions to the standard deviation of monthly mean temperature, this study has emphasized the typical energy budget features associated with temperature anomalies. Nevertheless, the correlation between the individual energy budget components and temperature anomalies is far from perfect (middle column of Fig. 3). Thus, a similar temperature anomaly may result from different combinations of energetic contributions. Examples of this variation are also readily visible in the time series of Fig. 1. For instance, although the net surface heat flux typically attenuates temperature variability, it amplified the cold anomalies in Januarys 2003 and 2010 (Fig. 2a, b). In both cases, the cold January was preceded in Finland by a very

cold second half of December, which served to reduce the ground-to-air heat flux by cooling the ground. Apart from this case-to-case variability, it would be worthwhile to study to which extent the relationship between energetics and temperature anomalies is (or is not) nonlinear. For example, do summer months with extreme warm anomalies differ from those with moderate anomalies in the relative importance of the energy balance components that contribute to these anomalies?

To give a globally consistent overview, the analysis in this paper has covered the whole world. More remains to be learned from more in-depth studies of temperature variability on regional scales. Moreover, keeping in mind the issues discussed in the previous section, a diagnostic energy budget approach should ideally be complemented by carefully designed model experiments. Such experiments could help to elucidate, for example, the remote effects of SST variability on the atmospheric energy transport and hence temperature.

Energetics of interannual temperature variability is also important in the context of climate modelling. The magnitude of interannual variability differs considerably between different global and regional climate models (Räisänen 2002; de Elía et al. 2013). Linking this variation to its energetic contributors could potentially help the improvement of climate models. The energetics point of view might also facilitate a better understanding of model-simulated future changes in temperature variability. Together with the evaluation of the present-day energetics of variability in the models, this could help distinguishing between more and less likely projections for the future.

**Acknowledgements** The author thanks the three reviewers for their constructive comments. This work was supported by the Academy of Finland Centre of Excellence in Atmospheric Science—From Molecular and Biological processes to the Global Climate (Luonnontieteiden ja Tekniikan Tutkimuksen Toimikunta, project 307331).

## Appendix A: Atmospheric energy flux convergence

The total energy in a hydrostatic air column is

$$E = \int_0^{p_s} (c_p T + Lq + k) \frac{dp}{g} + p_s h_s \quad (13)$$

where  $T$  is temperature,  $q$  specific humidity,  $k$  kinetic energy per unit mass,  $c_p$  specific heat of air at constant pressure,  $L$  the latent heat of vaporization,  $g$  the acceleration of gravity,  $p_s$  surface pressure and  $h_s$  the local surface height. We treat  $c_p = 1004 \text{ J kg}^{-1} \text{ K}^{-1}$ ,  $L = 2.5 \times 10^6 \text{ J kg}^{-1}$  and  $g = 9.81 \text{ m s}^{-1}$

as constants and neglect the effects of cloud water and ice. For a more precise formulation, see Mayer et al. (2017).

Differentiating (13) with respect to time gives

$$\frac{\partial E}{\partial T} = \int_0^{p_s} \frac{\partial e}{\partial T} \frac{dp}{g} + \left( \frac{e(p_s)}{g} + h_s \right) \frac{\partial p_s}{\partial t} \quad (14)$$

where  $e = c_p T + Lq + k$ . The latter term represents changes in atmospheric mass rather than in the energy content of air. It can be non-zero even with no net advection or diabatic source of energy within the air column, and is therefore neglected in our analysis (cf. Liang et al. 2017). An expression for  $\partial e / \partial t$  is obtained from the thermodynamic, momentum and specific humidity equations:

$$\frac{\partial e}{\partial t} = -\vec{U} \cdot \nabla_3(e + \Phi) + LS_q + Q - d \quad (15)$$

Here  $\vec{U}$  is three-dimensional wind,  $\nabla_3$  is three-dimensional gradient operator,  $\Phi$  is geopotential,  $S_q$  is net water vapour source per unit mass,  $Q$  is diabatic heating and  $d$  is dissipation of kinetic energy ( $d$  also contributes to  $Q$  and its net effect is therefore zero). Vertical integration of (15) gives

$$\int_0^{p_s} \frac{\partial e}{\partial T} \frac{dp}{g} = - \int_0^{p_s} \vec{U} \cdot \nabla_3(e + \Phi) \frac{dp}{g} + R_a + H + LE \quad (16)$$

where the mass-integrated water vapour source is assumed to equal the difference between surface evaporation ( $E$ ) and precipitation.  $R_a$  is the atmospheric radiation balance and  $H$  the sensible heat flux from the surface. Note that  $R_a + H + LE = S - L - G$  (Eqs. (1), (2)).

The first right-hand-side term in (16) represents the atmospheric energy flux convergence  $C$ , written in advection form. This term is usually converted to flux convergence form using the identity  $\vec{U} \cdot \nabla_3(e + \Phi) = \nabla_3 \cdot (\vec{U}(e + \Phi))$ , where we have used the continuity equation  $\nabla_3 \cdot \vec{U} = \nabla_p \cdot \vec{V} + \frac{\partial \omega}{\partial p} = 0$ . An advantage of this is that vertical flux convergence integrates to zero if vertical velocity at the surface can be neglected.

Furthermore, globally averaged horizontal convergence is zero, as required by energy conservation. On the other hand, the calculation of the energy flux convergence is numerically delicate. The main issue are errors in mass flux convergence, the effects of which can be reduced but not fully eliminated by adjusting the net mass flux to the air column (e.g., Hantel and Haase 1983; Chiodo and Haimberger 2010; Mayer and Haimberger 2012; Liu et al. 2017). After testing both the flux convergence and the advection form, we chose the latter since this yielded a better match between  $CONV$  and  $CONV_{DIR}$  in our implementation.

To study how atmospheric phenomena on different time scales contribute to the energy flux convergence, the monthly means of the advection term in (16) were further divided to two parts by writing

$$-\overline{\vec{U} \cdot \nabla_3(e + \Phi)} = -\underbrace{\overline{\vec{U} \cdot \nabla_3(\bar{e} + \bar{\Phi})}}_{MON} - \underbrace{\overline{\vec{U}' \cdot \nabla_3(e' + \Phi')}}_{SM} \quad (17)$$

where the overbar denotes the monthly mean and the prime a deviation from it. When integrated vertically and divided by  $D$ , these two components give  $CONV_{MON}$  and  $CONV_{SM}$  in (8). Similarly, dividing the left-hand-side term in (16) by  $D$  gives  $STOR$  in (8).

The energy flux convergence and the change in atmospheric energy content were evaluated using ERA-Interim data at 6-h time resolution, 0.75° horizontal resolution and 37 pressure levels. The results were then aggregated to the 2.5° grid used in the other parts of the analysis.

## Appendix B: Significance testing

The sign test is based on the count of positive and negative values of a variable. If both signs are equiprobable and autocorrelation is neglected, there is a 95.3% probability that the number of positive (or negative) values in a 37-year time series is within 13–24. Therefore, in a two-sided test, the same sign is required in at least 25 of the 37 years for statistical significance at 5% level.

When applying the sign test to SDCs, the obvious choice is to count the number of years in which the temperature anomaly associated with a given energy term agrees in sign with the actual temperature anomaly. However, averaging over calendar months requires normalization. From (9), the mean of  $SDC(i)$  over several calendar months is

$$[SDC(i)] = [r(i)SD(i)] = \left[ \frac{\text{cov}(\Delta T(i), \Delta T)}{SD(\Delta T)} \right] \quad (18)$$

where  $[\ ]$  denotes averaging over months and  $SD(\Delta T)$  and  $SD(i)$  are the standard deviations of temperature and its  $i$ :th energy balance component. Expanding the definition of covariance,

$$[SDC(i)] = \sum_{j=1}^N \left[ \frac{\Delta T(i)_j \Delta T_j}{SD(\Delta T)} \right] \equiv \sum_{j=1}^N f(i)_j \quad (19)$$

where  $N=37$  is the number of years. Thus, in the sign test, the positive and negative values of  $f(i)_j$  are counted.

### Appendix C: Decomposition of $LW_{CLEAR}$

The term  $LW_{CLEAR}$  represents variations in the clear-sky effective planetary emissivity defined as

$$\epsilon_{eff-CLEAR} = \frac{L_{CLEAR}}{\sigma T^4} \tag{20}$$

where  $L_{CLEAR}$  is the monthly mean clear-sky outgoing LW radiation and  $T$  is the monthly mean surface air temperature.

$\epsilon_{eff-CLEAR}$  can be further factored as

$$\epsilon_{eff-CLEAR} = \frac{L_{CLEAR}}{L_{S\uparrow}} \cdot \frac{L_{S\uparrow}}{\sigma T^4} \equiv \epsilon_A \epsilon_S \tag{21}$$

where  $L_{S\uparrow}$  is the upward LW flux at the surface.  $\epsilon_A$  is an inverse measure of the clear-sky atmospheric greenhouse effect, whereas  $\epsilon_S$  is an effective surface emissivity, which is affected by the actual surface emissivity, differences between the surface and surface air temperatures, and sub-monthly variations of temperature. The corresponding temperature anomalies are

$$LW_{CLEAR} = LW_{CLEAR-S} + LW_{CLEAR-A} \tag{22}$$

where

$$LW_{CLEAR-S} = -D^{-1} \Delta \epsilon_s [\epsilon_A] \sigma [T^4] \tag{23}$$

is the contribution from variations in effective surface emissivity and

$$LW_{CLEAR-A} = -D^{-1} \Delta \epsilon_A [\epsilon_S] \sigma [T^4] \tag{24}$$

represents the variations in the atmospheric clear-sky greenhouse effect.

$LW_{CLEAR-A}$  was further decomposed using the linear regression model

$$LW_{CLEAR-A} = \underbrace{a \Delta \sqrt{WWP}}_{LW_{CLEAR-WW}} + \underbrace{b \Delta (T_s - T_{300-700})}_{LW_{CLEAR-LR}} + \epsilon \tag{25}$$

where  $WWP$  is the vertically integrated water vapour path,  $T_s$  is surface temperature and  $T_{300-700}$  is the mean temperature at 300–700 hPa, broadly representing the layers from which most of the longwave radiation escapes to space under typical atmospheric conditions. The coefficients  $a$  and  $b$  were estimated from 37-year time series of monthly mean data for each of ERA-Interim and MERRA2, using the same values of  $a$  and  $b$  for all 12 months to avoid overfitting.  $\sqrt{WWP}$  was preferred over  $WWP$  since it explained a larger fraction of the variance in  $LW_{CLEAR-A}$  when used as the only predictor. This two-predictor model explains 83% (84%) of the globally averaged variance in  $LW_{CLEAR-A}$  in ERA-Interim (MERRA2), with  $\sqrt{WWP}$  alone explaining 61% (65%); see Fig. S14 for the geographical distribution of the explained

variance. As expected, the coefficients  $a$  and  $b$  in (25) are positive virtually everywhere (Fig. S15).

### References

Allan RP, Liu C, Loeb NG, Palmer MD, Roberts M, Smith D, Vidale P-L (2014) Changes in global net radiative imbalance 1985–2012. *Geophys Res Lett* 41:5588–5597

Andrews T, Webb MJ (2018) The dependence of global cloud and lapse-rate feedbacks on the spatial structure of tropical pacific warming. *J Clim* 31:641–654

Barriopedro D, Fischer EM, Luterbacher J, Trigo RM, García-Herrera R (2011) The hot summer of 2010: redrawing the temperature record map of Europe. *Science* 332:220–224

Bjerknes J (1964) Atlantic air–sea interaction. *Adv Geophys* 10:1–82

Black E, Blackburn M, Harrison G, Hoskins B, Methven J (2004) Factors contributing to the summer 2003 European heat wave. *Weather* 59:217–223

Chiodo G, Haimberger L (2010) Interannual changes in mass consistent energy budgets from ERA-Interim and satellite data. *J Geophys Res* 115:D02112

de Elia R, Biner S, Frigon A (2013) Interannual variability and expected regional climate change over North America. *Clim Dyn* 41:1245–1267

Dee DP et al (2011) The ERA-Interim reanalysis: configuration and performance of the data assimilation system. *Q J R Meteorol Soc* 137:553–597

Deser C, Blackmon MC (1993) Surface climate variations over the North Atlantic ocean during winter: 1900–1989. *J Clim* 6:1743–1753

Deser C, Thomas R, Alexander M, Lawrence D (2010) The seasonal atmospheric response to projected Arctic sea ice loss in the late twenty-first century. *J Clim* 23:333–351

Diaz HF, Hoerling MP, Eischeid JK (2001) ENSO variability, teleconnections and climate change. *Int J Climatol* 21:1845–1862

Fischer EM, Seneviratne SI, Lüthi D, Schär C (2007) Contribution of land-atmosphere coupling to recent European summer heat waves. *Geophys Res Lett* 34:L06707

García-Herrera R, Díaz J, Trigo RM, Luterbacher J, Fischer EM (2010) A review of the European summer heat wave of 2003. *Crit Rev Environ Sci Technol* 40:267–306

Gelaro R et al (2017) The modern-era retrospective analysis for research and applications, Version 2 (MERRA-2). *J Clim* 30:5419–5454

Hantel M, Haase S (1983) Mass consistent heat budget of the zonal atmosphere. *Bonner Meteorologische Abhandlungen* 29:87

Hedemann C, Mauritsen T, Jungclaus J, Marotzke J (2017) The subtle origins of surface-warming hiatuses. *Nat Clim Change* 7:336–340

Holmes CR, Woolling T, Hawkins E, de Vries H (2016) Robust future changes in temperature variability under greenhouse gas forcing and the relationship with thermal advection. *J Clim* 29:2221–2236

Holton JR, Hakim GJ (2012) An introduction to dynamic meteorology, 5th edn. Academic Press, Cambridge, pp 552

Hu X, Yang S, Cai M (2016) Contrasting the eastern Pacific El Niño and the central Pacific El Niño: process-based feedback attribution. *Clim Dyn* 47:2413–2424

Ji X, Neelin JD, Mechoso CR (2016) Baroclinic-to-barotropic pathway in El Niño—Southern Oscillation teleconnections from the viewpoint of a barotropic Rossby wave source. *J Atmos Sci* 73:4989–5002

Kara AB, Rochford PA, Hurlburt HE (2000) Efficient and accurate bulk parameterizations of air–sea fluxes for use in general circulation models. *J Atmos Ocean Technol* 17:1421–1438

- Kushnir Y (1994) Interdecadal variations in North Atlantic sea surface temperature and associated atmospheric conditions. *J Clim* 7:141–157
- Lau N-C, Holopainen EO (1984) Transient eddy forcing of the time-mean flow as identified by geopotential tendencies. *J Atmos Sci* 41:313–328
- Lau N-C, Nath MJ (1991) Variability of the baroclinic and barotropic transient eddy forcing associated with monthly changes in the midlatitude storm tracks. *J Atmos Sci* 48:2589–2613
- Liang M, Czaja A, Graverson R, Tailleux R (2017) Poleward energy transport: is the standard definition physically relevant at all time scales? *Clim Dyn*. <https://doi.org/10.1007/s00382-017-3722-x>
- Liu C, Allan RP, Mayer M, Hyder P, Loeb NG, Roberts CD, Valdivieso M, Edwards JM, Vidale P-L (2017) Evaluation of satellite and reanalysis-based global net surface energy flux and uncertainty estimates. *J Geophys Res Atmos* 122:6250–6272
- Loeb NG, Doelling DR, Wang H, Su W, Nguyen C, Corbett JG, Liang L, Mitrescu C, Rose FG, Kato S (2018) Clouds and the earth's radiant energy system (CERES) energy balanced and filled (EBAF) top-of-atmosphere (TOA) edition-4.0 data product. *J Clim* 31:895–918
- Lu J, Cai M (2009) A new framework for isolating individual feedback processes in coupled general circulation climate models. Part I: formulation. *Clim Dyn* 32:873–885
- Mayer M, Haimberger L (2012) Poleward atmospheric energy transports and their variability as evaluated from ECMWF reanalysis data. *J Clim* 25:734–752
- Mayer M, Haimberger L, Edwards JM, Hyder P (2017) Toward consistent diagnostics of the coupled atmosphere and ocean energy budgets. *J Clim* 30:9225–9246
- Paik S, Min S-K (2017) Climate responses to volcanic eruptions assessed from observations and CMIP5 multi-models. *Clim Dyn* 48:1017–1030
- Park T-W, Jeong J-H, Deng Y, Zhou R, Cai M (2015) Quantitative decomposition of radiative and non-radiative contributions to temperature anomalies related to siberian high variability. *Clim Dyn* 45:1207–1217
- Petrie RE, Shaffrey LC, Sutton RT (2015) Atmospheric impact of Arctic sea ice loss in a coupled ocean–atmosphere simulation. *J Clim* 28:9606–9622
- Picard G, Domine F, Krinner G, Arnaud L, Lefebvre E (2012) Inhibition of the positive snow-albedo feedback by precipitation in interior Antarctica. *Nat Clim Change* 2:795–798
- Räisänen J (2002) CO<sub>2</sub>-induced changes in interannual temperature and precipitation variability in 19 CMIP2 experiments. *J Clim* 15:2395–2411
- Räisänen J (2017) An energy balance perspective on regional CO<sub>2</sub>-induced temperature changes in CMIP5 models. *Clim Dyn* 48:3441–3454
- Randles CA et al (2017) The MERRA-2 aerosol reanalysis, 1980 onward. Part I: system description and data assimilation evaluation. *J Clim* 30:6823–6850
- Robock A (2000) Volcanic eruptions and climate. *Rev Geophys* 38:191–209
- Simmons AJ (1982) The forcing of stationary wave motion by tropical diabatic heating. *Q J R Meteorol Soc* 108:503–534
- Taylor KE, Crucifix M, Braconnot P, Hewitt CD, Doutriaux C, Broccoli AJ, Mitchell JFB, Webb MJ (2007) Estimating shortwave radiative forcing and response in climate models. *J Clim* 20:2530–2543
- Trenberth KE, Fasullo JT (2013) Regional energy and water cycles: transports from ocean to land. *J Clim* 26:7837–7851
- Trenberth KE, Shea DJ (2005) Relationships between precipitation and surface temperature. *Geophys Res Lett* 32:L14703
- Webb MJ, Slingo A, Stephens GL (1993) Seasonal variations of the clear-sky greenhouse effect: the role of changes in atmospheric temperatures and humidities. *Clim Dyn* 9:117–129
- Wells NC (2012) Atmosphere and ocean: a physical introduction. Wiley, New York, pp 442
- Wu R, Kirtman BP (2007) Regimes of seasonal air–sea interaction and implications for performance of forced simulations. *Clim Dyn* 29:393–410
- Yang X, DelSole T (2012) Systematic comparison of ENSO teleconnection patterns between models and observations. *J Clim* 25:425–446
- Yu B, Zhang X (2015) A physical analysis of the severe 2013/2014 cold winter in North America. *J Geophys Res* 120:10149–10165
- Zwiers FW, Kharin VV (1998) Intercomparison of interannual variability and potential predictability: an AMIP diagnostic subproject. *Clim Dyn* 14:517–528